Reducing beam hardening effects and metal artefacts in spectral CT using Medipix3RX

2014 JINST 9 P03015

(http://iopscience.iop.org/1748-0221/9/03/P03015)

PUBLISHED BY IOP PUBLISHING FOR SISSA MEDIALAB

RECEIVED: *November 21, 2013*
REVISED: *January 24, 2014*
ACCEPTED: *February 11, 2014*
PUBLISHED: *March 26, 2014*

Reducing beam hardening effects and metal artefacts in spectral CT using Medipix3RX

K. Rajendran,[a,1] **M.F. Walsh,**[a] **N.J.A. de Ruiter,**[a] **A.I. Chernoglazov,**[b] **R.K. Panta,**[a] **A.P.H. Butler,**[a,b,c,d] **P.H. Butler,**[b,c,d] **S.T. Bell,**[d] **N.G. Anderson,**[a] **T.B.F. Woodfield,**[a,b] **S.J. Tredinnick,**[b] **J.L. Healy,**[b] **C.J. Bateman,**[a] **R. Aamir,**[a] **R.M.N. Doesburg,**[b,c] **P.F. Renaud,**[b] **S.P. Gieseg,**[b] **D.J. Smithies,**[d] **J.L. Mohr,**[a] **V.B.H. Mandalika,**[b] **A.M.T. Opie,**[b] **N.J. Cook,**[e] **J.P. Ronaldson,**[a] **S.J. Nik,**[b] **A. Atharifard,**[a] **M. Clyne,**[f] **P.J. Bones,**[b] **C. Bartneck,**[b] **R. Grasset,**[b] **N. Schleich**[g] **and M. Billinghurst**[b]

[a] *University of Otago,*
2 Riccarton Ave, Christchurch 8140, New Zealand
[b] *University of Canterbury,*
Private Bag 4800, Christchurch 8140, New Zealand
[c] *The European Organization for Nuclear Research (CERN),*
Geneva, Switzerland
[d] *MARS Bioimaging Ltd,*
29a Clyde Rd, Christchurch, New Zealand
[e] *Canterbury District Health Board,*
Riccarton Avenue, PO Box 4710, Christchurch 8140, New Zealand
[f] *ILR,*
Christchurch, New Zealand
[g] *University of Otago,*
23A Mein Street, Newtown, Wellington 6021, New Zealand

E-mail: kishore.rajendran@canterbury.ac.nz

[1] Corresponding author.

doi:10.1088/1748-0221/9/03/P03015

2014 JINST 9 P03015

ABSTRACT: This paper discusses methods for reducing beam hardening effects and metal artefacts using spectral x-ray information in biomaterial samples. A small-animal spectral scanner was operated in the 15 to 80 keV x-ray energy range for this study. We use the photon-processing features of a CdTe-Medipix3RX ASIC in charge summing mode to reduce beam hardening and associated artefacts. We present spectral data collected for metal alloy samples, its analysis using algebraic 3D reconstruction software and volume visualisation using a custom volume rendering software. The cupping effect and streak artefacts are quantified in the spectral datasets. The results show reduction in beam hardening effects and metal artefacts in the narrow high energy range acquired using the spectroscopic detector. A post-reconstruction comparison between CdTe-Medipix3RX and Si-Medipix3.1 is discussed. The raw data and processed data are made available (http://hdl.handle.net/10092/8851) for testing with other software routines.

KEYWORDS: Medical-image reconstruction methods and algorithms, computer-aided diagnosis; X-ray detectors; Computerized Tomography (CT) and Computed Radiography (CR)

2014 JINST 9 P03015

Contents

2014 JINST 9 P03015

1 Introduction

Beam hardening artefacts in x-ray computed tomography (CT) of metal objects frequently limit the diagnostic quality in human imaging [1]. This applies to large objects such as orthopaedic implants and smaller samples like tissue-engineered scaffolds. The artefacts appear as bright and dark streaks and also as a cupping effect, affecting the metal and non-metal regions in the reconstructed image. During beam hardening, the mean energy of the x-ray beam increases, and dense metal samples can cause severe beam hardening due to reasonably high atomic number when compared to soft tissues. Metal objects also reduce the photon levels from the beam, thus starving the detector from receiving sufficient photons (photon starvation) and creating artefacts in the reconstructions. One common approach is to employ a source filter and preharden the beam, thus removing the low energy photons that largely contribute to beam hardening. Numerical correction techniques for beam hardening and metal artefacts have been reported, some of them used in clinical routines. These techniques include sinogram interpolation methods [2, 3], dual energy extrapolation [4], and energy models and polynomial corrections (for μCT) [5, 6]. Some of these post-processing techniques are computationally intense, requiring metal data segmentation and/or several forward and backward projections. Dual energy corrections are usually done at the cost of increased exposure [6].

Photon-counting detectors have been successfully employed in preclinical applications such as atheroma imaging [7, 8], targeted gold nanoparticle imaging [9] and luminal depiction in blood vessels [10]. In this paper, a novel approach towards minimising beam hardening effects using spectroscopic detectors is proposed. While Medipix has been reportedly used for non-destructive evaluation of polymer materials [11], to the best of our knowledge, beam hardening and metal artefact reduction using spectral imaging have not been reported. This study aims to minimise metal artefacts in the acquisition stage, by capturing the high energy quanta that exhibit lesser beam hardening effects. This property of high energy acquisition for reducing metal artefacts has been previously exploited in dual energy methods [4, 6]. The Medipix3 ASICs allow simultaneous

data acquisition from discrete energy ranges at a single exposure [12, 13]. The ASIC was designed to count photon events and categorise them based on energy thresholds specified by the user. This feature primarily enables the capture of spectral signatures for multiple materials which can be used for material discrimination. The number of counts for discrete energy bands can be obtained by subtracting data from two counters. This is carried out as a pre-processing step prior to flat-field normalization and reconstruction. The raw data from a counter has an energy range between [T_C, kVp], where T_C corresponds to the user-defined energy threshold and kVp is the maximum tube potential applied across the x-ray tube. Since the count information is acquired simultaneously, the noise in a particular energy range is the local Poisson noise due to quantum fluctuations. In addition, the high energy quanta that undergoes lesser beam hardening can be captured in a separate counter without additional exposure.

Earlier reports using Medipix detectors discuss the problem of charge sharing effects largely affecting the energy response [14, 15]. Charge sharing occurs when the charge carriers from a single photon event spread across the boundaries of multiple pixels and are counted as separate low energy events thereby distorting the spatial and spectral resolution. To overcome this problem, the new Medipix3RX enables a fully operational Charge Summing Mode (CSM) [12]. This mode is designed to perform alongside the fine pitch and spectroscopic configurations of the Medipix3 ASICs. The fine pitch configuration allows every pixel element to count independently with each pixel providing two counters. In spectroscopic (single cluster) mode, four pixels are grouped together as a single unit to provide eight counters at the cost of spatial resolution. In fine pitch with CSM, the charge deposited in every 4 pixels is reconstructed at the pixel corners (termed as summing nodes) and assigned to the pixel receiving the largest charge share. In spectroscopic configuration with CSM, four pixels are clustered to form a single unit. During charge sharing, a single event across multiple pixels is identified through inter-pixel communication. For a pixel pitch of 110 μm, the charge deposited in $220 \times 220\,\mu m^2$ area is reconstructed at individual cluster corners ($110 \times 110\,\mu m^2$ clusters) and assigned to a single cluster unit which has the highest contribution from the initial hit (figure 1). A spatial resolution of $110 \times 110\,\mu m^2$ is achieved, with 4 CSM counters (counting the summed charge) and 4 non-CSM counters.

The detection efficiency of high-Z sensors (like CdTe with 87.4% detection efficiency at 100 keV for 2 mm thickness [16]) make them suitable for operation in human diagnostic x-ray energy range [17]. The spectral acquisitions of metal samples made from titanium (Ti) and magnesium (Mg) alloys [18] are presented. Porous scaffolds of these metals are usually implanted in bone to study bone ingrowth [19, 20] and hence were chosen for this study due to its clinical relevance.

2 Materials and methods

For the study on beam hardening, we used a Medipix All Resolution System (MARS) [21] scanner. The scanner is equipped with a 2 mm CdTe sensor bump-bonded at 110 μm pitch to a Medipix3RX ASIC provided to us by X-ray Imaging Europe GmbH [22]. This allows the use of x-rays across the clinical energy spectrum upto 120 keV. All the acquisitions in this paper were carried out in spectroscopic configuration with CSM. The detector assembly is a module of the MARS camera which also contains a readout board, Peltier cooling system and an integrated bias-voltage board. A bias voltage of -750 V was applied across the sensor during the acquisitions. The MARS scanner

2014 JINST 9 P03015

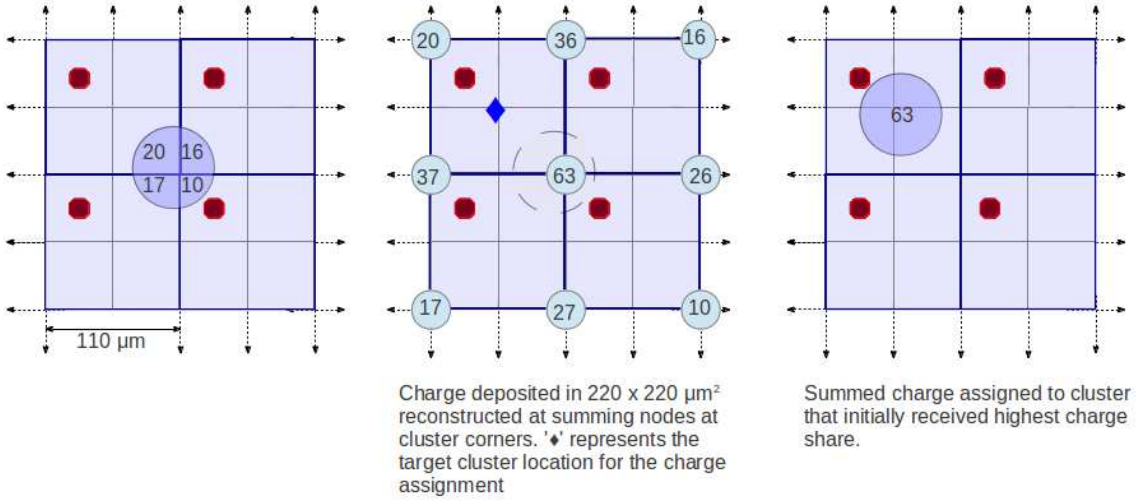

Figure 1. Illustration of CSM in spectroscopic configuration. A charge deposited over a $220 \times 220\,\mu m^2$ region is summed and assigned to the pixel unit receiving the highest charge share. The red octogons in every alternative pixel represent the pixel bond to the ASIC.

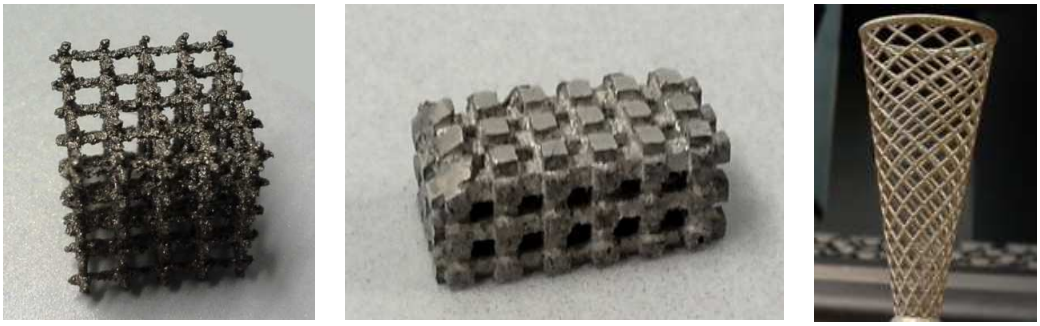

(a) Ti scaffold **(b)** Mg scaffold **(c)** Ti mesh

Figure 2. Photos of the metal samples (see table 1 for dimensions).

system comprises of the MARS camera, a rotating internal gantry and an x-ray source (Source-Ray SB-120-350, Source-Ray Inc, Ronkonkoma, NY) operated at 80 kVp. The source has an intrinsic 0.5 mm aluminium equivalent filtration. The focal spot size is 70 μm. Mechanical motor control (gantry rotation, source to detector translation, camera translation and sample translation), detector energy response calibration and threshold equalisation were performed using a custom built MARS scanner software. The samples used in this study are shown in figure 2 and their description is provided in table 1.

2.1 Threshold equalisation and energy calibration

A per-pixel threshold equalisation was performed using the electronic noise floor in each pixel as a threshold reference [23]. Two measured threshold points were subjected to a linear fit for estimating the adjustment value for a target threshold. Figure 3a shows two measured threshold values (100 and 75 DAC steps) on a single pixel for adjustment DAC step values of 0 and 5 on counter 1. The noise floor target was set at 10 DAC steps and the linear estimate for the adjustment

2014 JINST 9 P03015

Table 1. Sample description.

Sample	Material	Description
Metal phantom	Ti alloy	Solid cylinder of 8 mm diameter press fitted onto a polymethyl methacrylate (PMMA) cylinder of 25 mm diameter to study the cupping effect.
Porous scaffold	Ti alloy	Porous 3D lattice structure fabricated via electron beam melting with ≈700 μm thick struts. Used in tissue engineering research.
Porous scaffold	Mg alloy	Porous 3D lattice structure fabricated via an indirect additive manufacturing process in molten Mg with ≈500 μm thick struts. Used in tissue engineering research [18].
Porous mesh (stent-like pattern)	Ti alloy	Porous 3D structure fabricated via selective laser sintering with variable strut thickness between 620 μm and 670 μm. Sample length 45 mm.

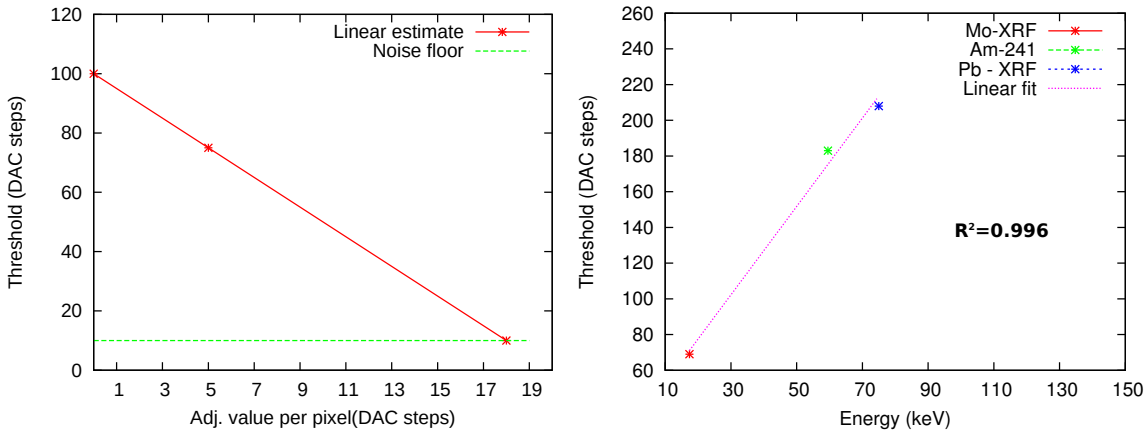

(a) Per-pixel threshold equalisation

(b) Energy calibration using XRF (Pb, Mo) and γ-ray (Am-241)

Figure 3. CdTe-Medipix3RX threshold equalisation and energy calibration.

value was projected at 18 DAC steps from the fit. This process is repeated across all 16,384 pixels for all the 4 counters.

The threshold DAC in the CdTe-Medipix3RX ASIC was calibrated against the reference energies such as x-ray fluorescence (XRF) emitted from metallic foils (Mo and Pb) and γ-rays emitted from an Am-241 radioisotope [24]. The energy response curve (figure 3b) shows a linear relationship between threshold DAC and the incident photon energy with $R^2 = 0.996$ between 17.4 keV to 75 keV. Based on this energy calibration, the noise floor was identified to have an upper limit at 10 keV.

2014 JINST 9 P03015

Table 2. Scan parameters.

Sample	SOD (mm)	SDD (mm)	Voltage (kVp)	Current (μA)	Exposure time (ms)
Ti phantom	166.2	251.4	80	60	80
Ti scaffold	166.2	251.4	80	60	80
Mg scaffold	130	215.2	80	25	80
Ti mesh	130	215.2	80	50	60

2.2 Spectral scan parameters

The scanner gantry was set to continuous-motion rotation to acquire projections at multiple camera positions. The CSM thresholds were set to 15, 35, 50 and 60 keV for the Ti samples and 15, 30, 40 and 50 keV for the Mg scaffold. Since Mg is a low-Z material ($Z = 12$) in comparison to Ti ($Z = 22$), relatively low exposure was used to avoid pulse pile-up effects [25, 26] and the thresholds were set sufficiently low to avoid photon starvation in the higher energy ranges. All the samples were mounted in air during the spectral scans. The MARS camera was translated vertically along the sample diameter to cover the entire vertical field of view, thereby providing projections from multiple camera positions. The number of projections per gantry rotation was set to 720. The geometric parameters (source to detector distance (SDD) and source to object distance (SOD)) and x-ray exposure settings are provided in table 2. For the Ti scaffold sample, a post-reconstruction comparison between a Si-Medipix3.1 (300 μm thick sensor layer) operating in Single Pixel Mode (SPM) with a pixel pitch of 55 μm and the CdTe-Medipix3RX operating in CSM was carried out. For the spectral acquisition with Si-Medipix3.1, the x-ray tube was operated at 50 kVp with a tube current of 300 μA and an exposure time of 150 ms. The thresholds were set to 15 and 30 keV.

2.3 Post processing chain

The raw data acquired from the scanner were flat-field normalized using open beam projections (600 frames per camera position). Dark-field images (64 frames per scan) were acquired for dark-field correction where pixels displaying counts with no incoming x-ray beam are identified and labelled as bad pixels. Also, there are inherent non-functional pixels due to sensor layer defects and bump-bonding failures which are labelled as dead pixels. A projection space statistical ring filter remotely based on [27] was applied prior to reconstruction. The projections were reconstructed using MARS-ART (Algebraic Reconstruction Technique) software [28]. The basic ART reconstruction model is given by

$$A.x(E) = b(E) \tag{2.1}$$

where A contains the geometric data, $x(E)$ is the energy-dependent volume of linear attenuation coefficients (to be estimated) and $b(E)$ is the energy-dependent transmission data. The MARS-ART software exploits the common geometry data to reconstruct all the energy ranges simultaneously. The $x(E)$ component is iteratively estimated using simultaneous algebraic reconstruction technique (SART) [29]. The software is customised to identify bad pixels and dead pixels, and ignore them during the reconstruction. Since the number of projections was set to 720, the dead pixel regions were compensated with oversampled data. The reconstruction model was provided with individual camera translation coordinates, and stitched projections that would be needed for filtered back

2014 JINST 9 P03015

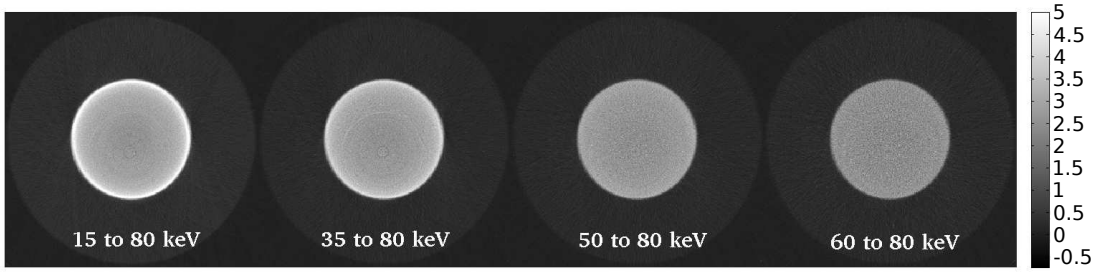

Figure 4. Spectral reconstruction of the Ti phantom (Magnification = 1.51, slice thickness = 1.05 mm). CNR between metal and PMMA regions is 5.1, 6.4, 8.9 and 7.3 for the four energy ranges respectively. The colour bar represents linear attenuation coefficients (cm^{-1}).

projection technique were not used. Volumetric rendering was performed using MARS-Exposure Render, which is a modified version of the open-source Exposure Render [30] software that implements a direct volume rendering (DVR) algorithm. Modifications to Exposure Render include the addition of tricubic B-spline interpolation between data voxels and the ability to simultaneously visualise up to 8 volumes.

3 Results and discussion

Figure 4 shows the spectral reconstruction of the Ti phantom. While wide energy ranges ($[15,80]$ keV and $[35,80]$ keV) were prone to cupping effect inhomogeneities, the narrow high energy ranges ($[50,80]$ keV and $[60,80]$ keV) exhibited less cupping effect. The gray level inhomogeneities are reflected in the Contrast to Noise Ratio (CNR). The CNR between metal and PMMA regions is relatively high in the last two energy ranges while the high variance in the metal region (figure 5) affects the global contrast in the energy ranges corresponding to $[15,80]$ keV and $[35,80]$ keV. The cupping effect reduction in higher energy ranges is further confirmed by the individual line profiles drawn from the spectral reconstructions.

A horizontal line profile passing through the origin of the metal cylinder reveals the level of cupping effect in the different energy ranges in figure 5. The 1D variance for the metal segment from the line profiles was calculated to determine the cupping effect inhomogeneities. The high energy range at $[60,80]$ keV showed almost a flat line profile in the metal segment with a gray level variance of $0.0330\,cm^{-2}$, confirming better homogeneity. While higher photon flux can improve the signal to noise ratio (SNR) in metal regions, it leads to per-pixel count rate saturation in open beam images and non-metal regions in the projections at low thresholds.

Figure 6 shows the spectral reconstruction of the Ti scaffold. While the contribution from low energy photons in the wide energy range ($[15,80]$ keV) resulted in bright streaks affecting the non-metal regions, high energy ranges ($[50,80]$ keV and $[60,80]$ keV) showed reduced artefacts. The CNR between the metal and non-metal regions improve in the higher energy ranges. Average attenuation coefficient in a region corresponding to air (within the scaffold) was calculated to be 0.905, 0.447, 0.191 and $0.134\,cm^{-1}$ in the four energy ranges respectively. The bright streaks in the lower energy ranges contribute to the increased gray values for air. Similar to the Ti phantom results, better CNR in the last two energy ranges ($[50,80]$ keV and $[60,80]$ keV) was achieved in

2014 JINST 9 P03015

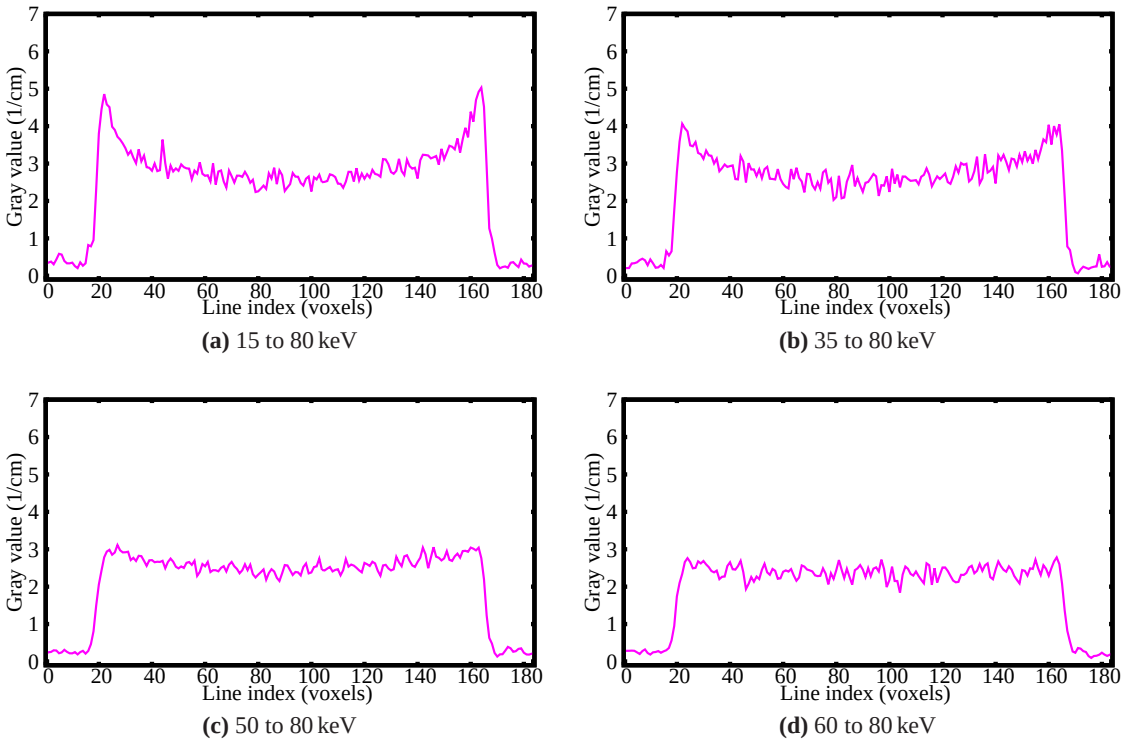

(a) 15 to 80 keV **(b)** 35 to 80 keV

(c) 50 to 80 keV **(d)** 60 to 80 keV

Figure 5. Line profiles from the spectral reconstruction of the Ti phantom. $\sigma^2_{\text{metal}} = 0.3061, 0.1790, 0.0432, 0.0330\,\text{cm}^{-2}$ for (a), (b), (c) and (d) respectively.

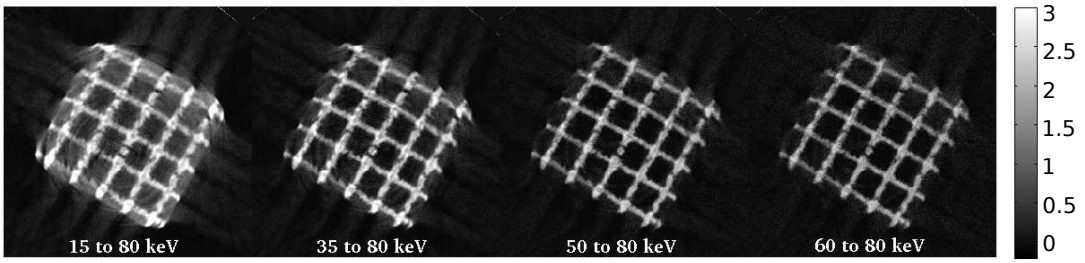

Figure 6. Spectral reconstruction of the Ti scaffold sample (Magnification = 1.51, slice thickness = 0.237 mm). CNR between metal and air (with bright streaks) in the energy ranges is 4.8, 5.4, 7.9, 8.1 respectively. The colour bar represents linear attenuation coefficients (cm^{-1}).

the absence of severe artefacts. Despite the visibility of minor streaks in the $[60,80]$ keV due to low photon counts, the artefacts were less pronounced when compared with the wide energy acquisition.

Figure 7 shows reconstructions for an energy range of $[30,50]$ keV obtained using Si-Medipix3.1 in SPM and an energy range of $[35,50]$ keV (subtracted energy range) using CdTe-Medipix3RX in CSM. The detection efficiency of Si (9.5% for 30 keV and 3.1% at 49.6 keV for 300 μm thickness [16]) is higher for lower energies whereas the detection efficiency of CdTe is relatively uniform for the chosen energy window ($\sim$ 99.9% between 30 and 50 keV for 2 mm thickness [16]). This can be related to the reconstructions obtained from the two different sensor

2014 JINST 9 P03015

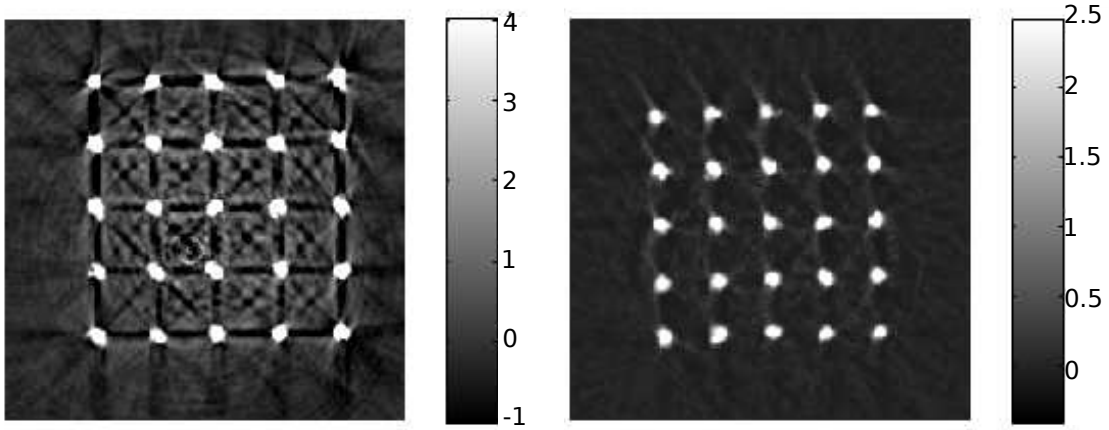

(a) 30 to 50 keV using Si Medipix3.1 **(b)** 35 to 50 keV using CdTe Medipix3RX

Figure 7. Ti scaffold reconstruction using Si Medipix3.1 and CdTe Medipix3RX. Regional gray level variances for a sample air region (with artefacts) are $0.934\,\mathrm{cm}^{-2}$ and $0.197\,\mathrm{cm}^{-2}$ for the reconstructions from Si and CdTe respectively. The colour bar represents linear attenuation coefficients (cm^{-1}).

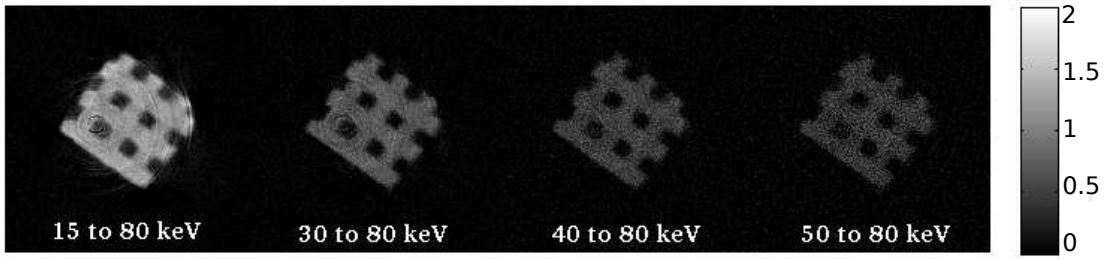

Figure 8. Spectral reconstruction of the Mg scaffold sample (Magnification = 1.65, slice thickness = 0.219 mm). CNR corresponding to the energy ranges is 8.3, 6.3, 4.2 and 2.7 respectively. The colour bar represents linear attenuation coefficients (cm^{-1}).

materials at approximately same energy windows, with the image from Si displaying increased streak artefacts. Due to poor detection efficiency of Si sensors, operation at higher energy ranges (> 50 keV) suitable for artefact reduction requires higher exposures.

Figure 8 shows the spectral reconstruction of the Mg scaffold. Minor streaks were visible in the $[15,80]$ keV range but this did not affect the CNR. The average attenuation coefficients for air region (with bright streaks) within the scaffold were calculated to be 0.292, 0.057, 0.023 and $0.012\,\mathrm{cm}^{-1}$ for the four energy ranges respectively. In scans involving smaller samples made from low-Z materials like Al or Mg, acquiring low energy quanta provides high CNR with minimal or no beam hardening effects while higher energy ranges, despite exhibiting no visible artefacts, have poor CNR. The increased noise level (background image noise $\sigma = 0.138\,\mathrm{cm}^{-1}$) in the higher energy range at $[50,80]$ keV relative to the wide energy range at $[15,80]$ keV (background image noise $\sigma = 0.094\,\mathrm{cm}^{-1}$) is due to relatively low photon counts in the higher energy range.

Figure 9 shows the spectral reconstruction for the Ti mesh sample. The gray level variance in the air region within the scaffold was calculated to be 0.04, 0.008, 0.006 and $0.008\,\mathrm{cm}^{-2}$ in the four energy ranges respectively. The wide energy range at $[15,80]$ keV suffers from artefacts

2014 JINST 9 P03015

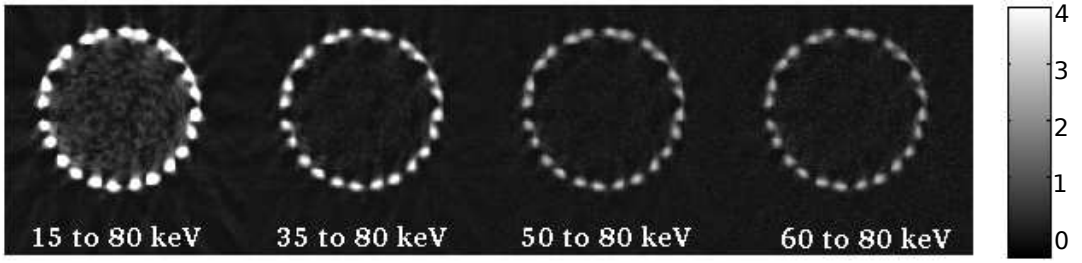

Figure 9. Spectral reconstruction of the Ti mesh sample (Magnification = 1.65, slice thickness = 0.222 mm). CNR for the energy ranges is 2.92, 2.71, 2.74 and 2.77. The colour bar represents linear attenuation coefficients (cm^{-1}).

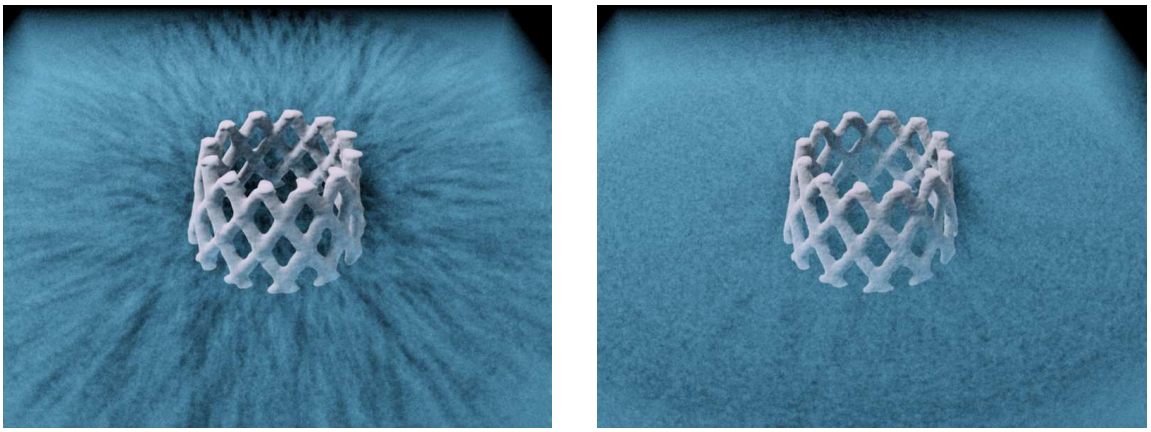

(a) 3D rendered volume using $[15,80]$ keV

(b) 3D rendered volume using $[50,80]$ keV

Figure 10. 3D visualisation of a segment from the Ti mesh sample. The blue region corresponds to air (false colour) with streak artefacts visible in the $[15,80]$ keV volume while the $[50,80]$ keV volume reveals relatively homogeneous air region with reduced artefacts.

in the non-metal regions. While the attenuation coefficients in the metal region for the image at $[15,80]$ keV are highest among the reconstructions (average $\mu_{\text{metal}} = 5.71$, 3.179, 2.051 and 1.773 cm^{-1} for the four energy ranges respectively), the CNR is affected due to the bright streaks present in the background. The reconstructions corresponding to $[35,80]$ keV, $[50,80]$ keV and $[60,80]$ keV provide a good trade-off between reduced artefact and CNR.

For the Ti mesh sample, the implications of streak artefacts affecting the surrounding non-metal region in 3D volume are visualised in figure 10. A metal segment from the Ti mesh (grey component) and the surrounding air region (blue component) is compared at two different energy ranges ($[15,80]$ keV and $[50,80]$ keV). While the wide energy range shows patterns of streak artefacts in the non-metal region, this is minimised in the higher energy range at $[50,80]$ keV which shows relatively homogeneous non-metal region. While we illustrate the extent of streak artefacts in the air region, this can be translated to a clinical scenario where surrounding low contrast soft tissue regions in the image are prone to streak artefacts. The $[50,80]$ keV volume shows reduced streaks and the metal to non-metal contrast is similar to that of the reconstruction from $[15,80]$ keV as illustrated in figure 9.

2014 JINST 9 P03015

4 Conclusion

We have demonstrated the use of spectral x-ray imaging in reducing beam hardening effects and metal artefacts. Multi-energy acquisition of metal samples has the added advantage of capturing spectral information which exhibits reduced artefacts and subsequently better CNR. Further improvements in metal artefact reduction should be achieved by (i) increasing the x-ray tube potential from 80 kVp to 120 kVp and (ii) by correcting the metal regions in wide energy ranges using the high energy range as a reference. Since the soft-tissue around metal hardware is of clinical interest, accurate material discrimination using spectral CT requires artefact free non-metal information across all energy ranges. Different metal samples and scaffold structures are currently being studied using the MARS spectral imaging modality. Tissue ingrowth quantification using imaging techniques will help in non-destructive evaluation of the biomaterials used.

The post-reconstruction comparison between CdTe and Si Medipix detectors described in this paper reveals the suitability of high-Z sensor materials for clinical imaging requiring high detection efficiency in a wider range of x-ray energies. The raw data (dicom files), pre-processed projection images and the reconstructions are made available (http://hdl.handle.net/10092/8851) for readers to test the data using their familiar routines.

Acknowledgments

This project was funded by Ministry of Business, Innovation and Employment (MBIE), New Zealand under contract number UOCX0805. The authors would like to thank all members of MARS-CT project, the Medipix2 collaboration, and the Medipix3 collaboration. In particular we acknowledge the CERN based designers Michael Campbell, Lukas Tlustos, Xavier Llopart, Rafael Ballabriga and Winnie Wong, and the material scientists Alex Fauler, Simon Procz, Elias Hamann, Martin Pichotka, and Michael Fiederle from Freiburger Materialforschungszentrum (FMF) and X-ray Imaging Europe GmbH. We also thank Graeme Kershaw, University of Canterbury for preparing the hardware phantom, and Anton Angelo, University of Canterbury for co-ordinating access to the data repository.

References

[1] J.F. Barrett and N. Keat, *Artifacts in CT: recognition and avoidance*, *Radiographics* **24** (2004) 1679.

[2] E. Meyer, R. Raupach, M. Lell, B. Schmidt and M. Kachelrieß, *Normalized metal artifact reduction (NMAR) in computed tomography*, *Med. Phys.* **37** (2010) 5482.

[3] E. Meyer, R. Raupach, M. Lell, B. Schmidt and M. Kachelrieß, *Frequency split metal artifact reduction (FSMAR) in computed tomography*, *Med. Phys.* **39** (2012) 1904.

[4] F. Bamberg et al., *Metal artifact reduction by dual energy computed tomography using monoenergetic extrapolation*, *Eur. Radiol.* **21** (2011) 1424.

[5] E. Van de Casteele, D. Van Dyck, J. Sijbers and E. Raman, *An energy-based beam hardening model in tomography*, *Phys. Med. Biol.* **47** (2002) 4181.

[6] E. Van de Casteele, D. Van Dyck, J. Sijbers and E. Raman, *A model-based correction method for beam hardening artefacts in X-ray microtomography*, *J. X-Ray Sci. Technol.* **12** (2004) 43.

2014 JINST 9 P03015

[7] J.P. Ronaldson et al., *Toward quantifying the composition of soft tissues by spectral CT with Medipix3*, *Med. Phys.* **39** (2012) 6847.

[8] R. Zainon et al., *Spectral CT of carotid atherosclerotic plaque: comparison with histology*, *Eur. Radiol.* **22** (2012) 2581.

[9] D.P. Cormode et al., *Atherosclerotic plaque composition: analysis with multicolor CT and targeted gold nanoparticles*, *Radiology* **256** (2010) 774.

[10] S. Feuerlein et al., *Multienergy photon-counting k-edge imaging: potential for improved luminal depiction in vascular imaging*, *Radiology* **249** (2008) 1010.

[11] S. Procz et al., *Medipix3 CT for material sciences*, 2013 *JINST* **8** C01025.

[12] R. Ballabriga et al., *The Medipix3RX: a high resolution, zero dead-time pixel detector readout chip allowing spectroscopic imaging*, 2013 *JINST* **8** C02016.

[13] M.F. Walsh et al., *Spectral CT data acquisition with Medipix3.1*, 2013 *JINST* **8** P10012.

[14] H. Zeller et al., *Charge sharing between pixels in the spectral Medipix2 X-ray detector*, *IVCNZ '09* (2009) 363.

[15] M. Chmeissani et al., *Charge sharing measurements of pixilated CdTe using Medipix-II chip*, *IEEE IMTC 04* **1** (2004) 787.

[16] M. Berger et al., *NIST-XCOM: photon cross sections database* (2011).

[17] T. Takahashi and S. Watanabe, *Recent progress in CdTe and CdZnTe detectors*, *IEEE Trans. Nucl. Sci.* **48** (2001) 950.

[18] T.L. Nguyen, M.P. Staiger, G.J. Dias and T.B.F. Woodfield, *A novel manufacturing route for fabrication of topologically-ordered porous magnesium scaffolds*, *Adv. Eng. Mater.* **13** (2011) 872.

[19] P. Habibovic, T. Woodfield, K. Groot and C. Blitterswijk, *Predictive value of in vitro and in vivo assays in bone and cartilage repair — what do they really tell us about the clinical performance?*, J. Fisher ed., Advances in Experimental Medicine and Biology, Springer, *Tissue Eng.* **585** (2007) 327.

[20] J.E. Biemond, G. Hannink, N. Verdonschot and P. Buma, *Bone ingrowth potential of electron beam and selective laser melting produced trabecular-like implant surfaces with and without a biomimetic coating*, *J. Mater. Sci. Mater. M.* **24** (2013) 745.

[21] M.F. Walsh et al., *First CT using Medipix3 and the MARS-CT-3 spectral scanner*, 2011 *JINST* **6** C01095.

[22] *X-ray Imaging Europe GmbH*, http://www.xi-europe.de (2012).

[23] M.F. Walsh, *Spectral computed tomography development*, Ph.D. Thesis, University of Otago (2013).

[24] R.K. Panta et al., *Energy resolving performance of a CdTe-Medipix3RX spectroscopic X-ray detector*, in preparation.

[25] H.-M. Cho et al., *The effects of photon flux on energy spectra and imaging characteristics in a photon-counting X-ray detector*, *Phys. Med. Biol.* **58** (2013) 4865.

[26] R. Aamir et al., *Pixel sensitivity variations in a CdTe-Medipix2 detector using poly-energetic X-rays*, 2011 *JINST* **6** C01059.

[27] J. Sijbers and A. Postnov, *Reduction of ring artefacts in high resolution micro-CT reconstructions*, *Phys. Med. Biol.* **49** (2004) N247.

[28] N.D. Tang et al., *Using algebraic reconstruction in computed tomography*, *IVCNZ '12* (2012) 216.

[29] A.H. Andersen and A.C. Kak, *Simultaneous algebraic reconstruction technique (SART): a superior implementation of the art algorithm*, *Ultrasonic Imaging* **6** (1984) 81.

[30] T. Kroes, F.H. Post and C.P. Botha, *Exposure render: an interactive photo-realistic volume rendering framework*, *PLoS ONE* **7** (2012) e38586.

2014 JINST 9 P03015